

Article

# Hydrothermal and Entropy Investigation of Ag/MgO/H<sub>2</sub>O Hybrid Nanofluid Natural Convection in a Novel Shape of Porous Cavity

Nidal Abu-Libdeh <sup>1,\*</sup>, Fares Redouane <sup>2</sup>, Abderrahmane Aissa <sup>3</sup> , Fateh Mebarek-Oudina <sup>4</sup> , Ahmad Almuhtady <sup>5</sup> , Wasim Jamshed <sup>6</sup> and Wael Al-Kouz <sup>7</sup>

<sup>1</sup> Department of Mathematics and Natural Sciences, College of Sciences and Human Studies, Prince Mohammad Bin Fahd University, Al Khobar 31952, Saudi Arabia

<sup>2</sup> LGIDD, Department of Physics, Faculty of SESNV, Ahmed ZABANA University, Relizane 48000, Algeria; redouane.fares@cu-relizane.dz

<sup>3</sup> Laboratoire de Physique Quantique de la Matière et Modélisation Mathématique (LPQ3M), University of Mascara, Mascara 29000, Algeria; a.aissa@univ-mascara.dz

<sup>4</sup> Department of Physics, Faculty of Sciences, University of 20 août 1955—Skikda, Skikda 21000, Algeria; f.mebarek\_oudina@univ-skikda.dz

<sup>5</sup> Mechanical & Maintenance Engineering Department, School of Applied Technical Sciences, German Jordanian University, Amman 11180, Jordan; ahmad.almuhtady@gju.edu.jo

<sup>6</sup> Department of Mathematics, Capital University of Science and Technology (CUST), Islamabad 44000, Pakistan; dmt143004@cust.pk

<sup>7</sup> Department of Mechanical Engineering, College of Engineering, Prince Mohammad Bin Fahd University, Al Khobar 31952, Saudi Arabia; walkouz@pmu.edu.sa

\* Correspondence: nabulibdeh@pmu.edu.sa



**Citation:** Abu-Libdeh, N.; Redouane, F.; Aissa, A.; Mebarek-Oudina, F.; Almuhtady, A.; Jamshed, W.; Al-Kouz, W. Hydrothermal and Entropy Investigation of Ag/MgO/H<sub>2</sub>O Hybrid Nanofluid Natural Convection in a Novel Shape of Porous Cavity. *Appl. Sci.* **2021**, *11*, 1722. <https://doi.org/10.3390/app11041722>

Academic Editor: Andrea Frazzica  
Received: 7 January 2021  
Accepted: 9 February 2021  
Published: 15 February 2021

**Publisher's Note:** MDPI stays neutral with regard to jurisdictional claims in published maps and institutional affiliations.



**Copyright:** © 2021 by the authors. Licensee MDPI, Basel, Switzerland. This article is an open access article distributed under the terms and conditions of the Creative Commons Attribution (CC BY) license (<https://creativecommons.org/licenses/by/4.0/>).

**Abstract:** In this study, a new cavity form filled under a constant magnetic field by Ag/MgO/H<sub>2</sub>O nanofluids and porous media consistent with natural convection and total entropy is examined. The nanofluid flow is considered to be laminar and incompressible, while the advection inertia effect in the porous layer is taken into account by adopting the Darcy–Forchheimer model. The problem is explained in the dimensionless form of the governing equations and solved by the finite element method. The results of the values of Darcy (Da), Hartmann (Ha) and Rayleigh (Ra) numbers, porosity ( $\varepsilon_p$ ), and the properties of solid volume fraction ( $\phi$ ) and flow fields were studied. The findings show that with each improvement in the Ha number, the heat transfer rate becomes more limited, and thus the magnetic field can be used as an outstanding heat transfer controller.

**Keywords:** natural convection; entropy; hybrid nanofluids; magnetic field; porous media

## 1. Introduction

Over the past two decades, as a relatively recent type of heat transfer fluid, nanofluids have attracted the interest of researchers throughout the world. In the mechanical and chemical engineering disciplines, as well as physics and material sciences, the ever-increasing number of journal and conference papers, as well as several books devoted to nanofluids, have made them one of the top hot topics. For the first time, Choi and Eastman [1] introduced nanofluids to increase the thermal transfer of cooling systems. Maxwell [2] suggested, for the first time in the nineteenth century, the key concept of retaining very tiny particles in standard fluid to obtain desired physical properties. He assumed that by dispersing metal ions in water, physical characteristics could be improved. Unfortunately, because of the rapid sedimentation of microparticles, he did not explain his theory. To boost thermophysical properties such as density, viscosity, precise heat transfer, and thermal conductivity, nanofluids apply to nanoscale particles suspended in traditional heat transfer fluids such as ethylene glycol, oil, and water. Nanofluid applications are now

encountered successfully in a wide variety of sectors, including, though not limited to, impingement jets, heat exchangers, clean energy, automobiles, electronic chip cooling, nuclear reactors, heating and tempering, combustion, lubrication, and medication [3–9]. Patterson and Imberger [10] claimed to have undertaken one of the first studies on the movement of fluid inside enclosures. Inside a rectangular enclosure, they analyzed transient natural convection. They concluded that while the steady state of the flows analyzed does not depend on the value of the Prandtl number ( $Pr$ ) which represents the ratio of the viscosity to the thermal diffusivity of the fluid, it is apparent that the unsteady flows can be heavily dependent on the Prandtl number. Then, different unstable flows contribute to different regimes but ultimately converge into the same stable states. Armaghani et al. [11] studied, numerically, alumina/ $H_2O$  nanofluid natural convection inside a puzzled L-shaped ring. They reported that any increase in aspect ratio improved heat transfer and the strength of nanofluids. Malekpour et al. [12] studied, numerically, the production of entropy and magnetic natural copper oxide/ $H_2O$  nanofluid convection inside an I-shaped enclosure. Their findings found that the volume concentration of nanoparticles improved normal convection but increased the rate of entropy production unfavorably. In addition, they found that both the rate of entropy production and natural convection could be repressed by the magnetic field.

Mamourian et al. [13] attempted to research the effect of a magnetic field and its angles of inclination on the heat transfer of natural convection and the production of entropy of nanofluids in a square cavity. They discovered that by increasing the Rayleigh ( $Ra$ ) number, the overall entropy production and the mean Nusselt number ( $Nu_{avg}$ ) increased, independent of the Hartmann ( $Ha$ ) number and inclination angle.

Bondareva et al. [14] investigated the magnetic natural convection inside a filled cavity of inclined wavy transparent porous nanofluids in another numerical analysis. Their observations indicated that a reciprocal increase in the  $Ha$  number and the angle of inclination of the magnetic field induced a decrease in heat transfer and attenuation of convective flow.

Recently, Dogonchi et al. [15] examined the magnetic natural convection of nanofluids within a cavity with an inclined elliptical radiator. They tried to find the effect of nanoparticle form factors, such as copper cubic, cylindrical, and platelet shapes, on heat transfer and they discovered that from the perspective of heat transfer enhancement, the platelet nanoparticle was stronger than the other shapes. Their findings indicate that by increasing nanoparticle volume concentration, the heat transfer increases.

The entropy production and magnetic natural convection of a nanofluid inside an inclined square porous enclosure were investigated numerically by Rashad et al. [16]. They also studied the influence of the scale and position of the source and heat sink. Their findings showed, unexpectedly, that the amount of Nusselt decreased with each increase in the volume fraction of the nanoparticle as well as the  $Ha$  number.

More recently, Sajjadi et al. [17] studied the magnetic natural convection of a hybrid nanofluid in a porous medium inside a square cavity. Their findings showed that the rate of heat transfer was decreased by increasing the magnetic field and this decrease was minimized by the value of Darcy ( $Da$ ) number and boosted by the value of the  $Ra$  number and porosity ( $\epsilon_p$ ).

The magnetic natural convection of nanofluids ( $H_2O$ /copper) in a porous arc-shaped enclosure was investigated by Dogonchi et al. [18], considering Brownian motion as an important mechanism for increasing heat transfer. Their observations showed that the frequency of the convective flow had a favorable relationship with the values of the  $Da$  and  $Ra$  numbers, whereas it has an opposite relationship with the magnetic field angle of inclination and the  $Ha$  number.

There have also been other worthwhile numerical investigations [19–35] about natural convection. In many sectors, such as mobile devices, including varied geometries and functions, traditional nanofluids, as well as their new version dubbed “hybrid nanofluids”,

are importance to thermal scientists and researchers around the world for supporting cooling processes.

The aforementioned studies in the literature investigated different cavity configurations with many physical effects including the effect of magnetic field and porous media. Moreover, these studies have helped researchers in terms of the range of investigated parameters as well as the selection of innovative examined geometry. A trapezoid, which is analyzed in this paper, is one such geometry that is used for cooling purposes. This geometry is more realistic than the cavities in the rectangle. Therefore, in this paper, we investigate the natural convection heat transfer of Ag/MgO/water nanofluids in a porous cavity subjected to a constant magnetic field. The effects of diverse controlling parameters such as  $Da$ ,  $Ha$ , and  $Ra$  numbers,  $\varepsilon_p$  on flow, and heat transfer characteristics with entropy are examined.

## 2. Problem Description

Natural convection of Ag/MgO/water nanofluids in a porous enclosure under constant horizontal magnetic field is shown in Figure 1. The effects of gravity, the conduction and convection heat transfer, as well as the external magnetic field on the flow are examined and analyzed thoroughly. The figure also shows that the cavity is of length  $L$  and height  $H$ . The hot surface is set at a  $T_h$ , while the cold surfaces are set at  $T_c$ . The mesh of the study's domain is illustrated in Figure 2. The cavity is filled with a porous medium and subjected to a magnetic field ( $B_0$ ).

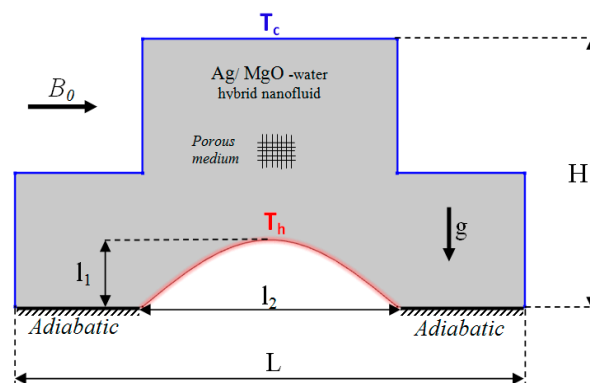


Figure 1. The geometry of the physical model.

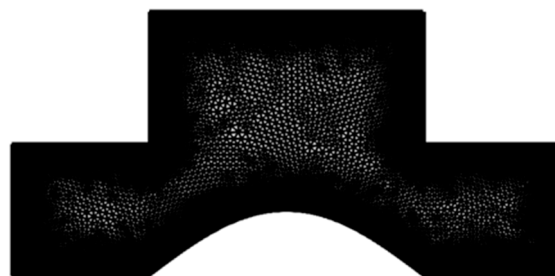


Figure 2. Mesh of the model.

## 3. Formulation of the Mathematical Model

### 3.1. Governing Equations and Boundary Conditions

The stationary natural Magnetohydrodynamics (MHD) convection flow is analyzed through a novel shape of porous cavity for hybrid nanofluid. For modeling a porous medium, the model of Brinkman–Forchheimeris used [36]. Navier–Stokes and heat equa-

tions, expressed in Cartesian coordinates for the problem taking into account the above assumptions, can be formulated as follows:

$$\frac{\partial u}{\partial x} + \frac{\partial v}{\partial y} = 0 \tag{1}$$

$$\frac{1}{\varepsilon_p^2} \left( u \frac{\partial u}{\partial x} + v \frac{\partial u}{\partial y} \right) = -\frac{1}{\rho_{nf}} \frac{\partial p}{\partial x} + \frac{\nu_{nf}}{\varepsilon_p} \left( \frac{\partial^2 u}{\partial x^2} + \frac{\partial^2 u}{\partial y^2} \right) - \nu_{nf} \frac{u}{K} - \frac{F_c}{\sqrt{K}} |u| \tag{2}$$

$$\frac{1}{\varepsilon_p^2} \left( u \frac{\partial v}{\partial x} + v \frac{\partial v}{\partial y} \right) = -\frac{1}{\rho_{nf}} \frac{\partial p}{\partial y} + \frac{\nu_{nf}}{\varepsilon_p} \left( \frac{\partial^2 v}{\partial x^2} + \frac{\partial^2 v}{\partial y^2} \right) - \nu_{nf} \frac{v}{K} - \frac{F_c}{\sqrt{K}} v |u| + \beta_{nf} g (T - T_{avg}) + \frac{\sigma_{nf}}{\rho_{nf}} B_0^2 v \tag{3}$$

$$u \frac{\partial T}{\partial x} + v \frac{\partial T}{\partial y} = \alpha_{nf} \left( \frac{\partial^2 T}{\partial x^2} + \frac{\partial^2 T}{\partial y^2} \right) \tag{4}$$

where  $\alpha_{nf} = \frac{k_{nf}}{(\rho c_p)_{nf}}$  is the thermal diffusivity of the nanofluid,  $|u| = \sqrt{u^2 + v^2}$  amplitude velocity.  $F_c = \frac{b}{\sqrt{a} \varepsilon^{3/2}}$  denotes the Forchheimer coefficient (where  $a = 150$  and  $b = 1.75$ ) and demonstrates the operative thermal conductivity of porous medium saturated with nanofluid, where the porous medium  $K$  is the permeability and  $\varepsilon_p$  is the porosity of the medium, that can be described as follows [37]:

$$K = \frac{\varepsilon_p^3 d_m^2}{150(1 - \varepsilon_p)^2} \tag{5}$$

For the base fluid and nanoparticles, Table 1 exhibits the thermophysical properties.

**Table 1.** Thermophysical properties of the nanoparticles and the fluid (Ag/MgO/water (50:50)) [37].

Physical Properties	$C_p$ (J/kg·K)	$k$ (W/m·k)	$\rho$ (kg/m <sup>3</sup> )	$\beta \cdot 10^{-5}$ (K <sup>-1</sup> )	$\sigma$ (s/m)	$\alpha$ (m <sup>2</sup> /s)
Water	4179	0.613	997.1	21	$5.5 \times 10^{-6}$	$1.47 \times 10^{-7}$
Ag	235	429	10500	5.4	$8.1 \times 10^{-4}$	$147 \times 10^{-3}$
MgO	879	30	3580	3.36	$8 \times 10^{-4}$	$95.3 \times 10^{-7}$

The following nondimensional variables are employed to transform these governing equations:

$$X = \frac{x}{L}, Y = \frac{y}{L}, U = \frac{u \cdot L}{\alpha_{bf}}, V = \frac{v \cdot L}{\alpha_{bf}}, \theta = \frac{T - T_f}{T_h - T_f}, P = \frac{(p + \rho_{0bf} g y) L^2}{\rho_{bf} \alpha_{bf}^2} \tag{6}$$

Dimensionless numbers are written as:

$$Pr = \frac{\nu_{bf}}{\alpha_{bf}}, Da = \frac{K}{L^2}, Ha = LB_0 \sqrt{\frac{\sigma_{bf}}{\mu_{bf}}}, Ra = \frac{\beta_{bf} g (T_h - T_c) L^3}{\alpha_{bf} \nu_{bf}} \tag{7}$$

The nondimensional governing equations form as follows:

$$\frac{\partial U}{\partial X} + \frac{\partial V}{\partial Y} = 0 \tag{8}$$

$$\frac{1}{\varepsilon_p^2} \frac{\rho_{nf}}{\rho_{bf}} \left( U \frac{\partial U}{\partial X} + V \frac{\partial U}{\partial Y} \right) = -\frac{\partial P}{\partial X} + \frac{1}{\varepsilon_p} \frac{\nu_{nf}}{\nu_{bf}} \frac{Pr}{\sqrt{Ra}} \left( \frac{\partial^2 U}{\partial X^2} + \frac{\partial^2 U}{\partial Y^2} \right) - \frac{\nu_{nf}}{\nu_{bf}} \frac{Pr}{Da \sqrt{Ra}} U - \frac{F_c}{\sqrt{Da}} |U| \tag{9}$$

$$\frac{1}{\varepsilon_p^2} \frac{\rho_{nf}}{\rho_{bf}} \left( U \frac{\partial V}{\partial X} + V \frac{\partial V}{\partial Y} \right) = -\frac{\partial P}{\partial Y} + \frac{1}{\varepsilon_p} \frac{\nu_{nf}}{\nu_{bf}} \frac{Pr}{\sqrt{Ra}} \left( \frac{\partial^2 V}{\partial X^2} + \frac{\partial^2 V}{\partial Y^2} \right) - \frac{\nu_{nf}}{\nu_{bf}} \frac{Pr}{Da \sqrt{Ra}} V - \frac{F_c}{\sqrt{Da}} |U| V + Pr \frac{\beta_{nf}}{\beta_f} g \theta + \frac{\sigma_{nf}}{\rho_{nf}} \frac{\rho_f}{\rho_{nf}} \frac{Pr}{\varepsilon_p \sqrt{Ra}} V \tag{10}$$

$$U \frac{\partial \theta}{\partial X} + V \frac{\partial \theta}{\partial Y} = \frac{\sigma_{nf}}{\sigma_{bf}} \left( \frac{\partial^2 \theta}{\partial X^2} + \frac{\partial^2 \theta}{\partial Y^2} \right) \tag{11}$$

For the computational domain of proper boundary conditions, the dimensional form represented for walls as follows:

- The outer wall  $u = v = 0, T = T_c$
- The mi sphere wall  $u = v = 0, T = T_h$
- The down walls

$$u = v = 0, \frac{\partial T}{\partial n} = 0 \tag{12}$$

### 3.2. Thermophysical Properties of the Nanofluid

Designed for nanoparticles MgO and Ag, the properties are obtained [38] as follows:

$$\varphi = \varphi_{Ag} + \varphi_{Mgo} \tag{13}$$

$$\rho_{np} = \frac{\varphi_{Mgo} \rho_{Mgo} + \varphi_{Ag} \rho_{Ag}}{\varphi} \tag{14}$$

$$(c_p)_{np} = \frac{\varphi_{Mgo} (c_p)_{Mgo} + \varphi_{Ag} (c_p)_{Ag}}{\varphi} \tag{15}$$

$$\beta_{np} = \frac{\varphi_{Mgo} \beta_{Mgo} + \varphi_{Ag} \beta_{Ag}}{\varphi} \tag{16}$$

$$k_{np} = \frac{\varphi_{Mgo} k_{Mgo} + \varphi_{Ag} k_{Ag}}{\varphi} \tag{17}$$

$$\sigma_{np} = \frac{\varphi_{Ag} \sigma_{Ag} + \varphi_{Mgo} \sigma_{Mgo}}{\varphi} \tag{18}$$

The thermal conductivity, heat capacity, and density of the nanofluid can be calculated as follows [39]:

$$\sigma_{hnf} = (1 - \varphi) \sigma_{bf} + \varphi \sigma_{np} \tag{19}$$

$$\rho_{hnf} = (1 - \varphi) \rho_{bf} + \varphi \rho_{np} \tag{20}$$

$$(\rho\beta)_{hnf} = (1 - \varphi) (\rho\beta)_{bf} + \varphi (\rho\beta)_{np} \tag{21}$$

$$(\rho c_p)_{hnf} = (1 - \varphi) (\rho c_p)_{bf} + \varphi (\rho c_p)_{np} \tag{22}$$

$$\alpha_{hnf} = \frac{k_{hnf}}{(\rho c_p)_{hnf}} \tag{23}$$

$$\frac{k_{hnf}}{k_{bf}} = \frac{k_{np} + (n - 1)k_{bf} - (n - 1)(k_{bf} - k_{np})\varphi}{k_{np} + (n - 1)k_{bf} + (k_{bf} - k_{np})\varphi} \tag{24}$$

The effective dynamic viscosity based on the Brinkman mode is considered as follows:

$$\mu_{hnf} = \frac{\mu_{bf}}{(1 - \varphi)^{2.5}} \tag{25}$$

$$\frac{\sigma_{hnf}}{\sigma_{bf}} = 1 + \frac{3(\sigma_{np} - \sigma_{bf})\varphi}{(\sigma_{np} + 2\sigma_{bf}) - (\sigma_{np} - \sigma_{bf})\varphi} \tag{26}$$

The local and average Nusselt numbers along the heated wall can be defined as:

$$Nu_{loc} = \frac{k_{hnf}}{k_{bf}} \frac{\partial T}{\partial y} \quad (27)$$

$$Nu_{avg} = \frac{1}{L} \int_0^L Nu_{loc} dL \quad (28)$$

### 3.3. Nondimensional Entropy Generation

Local entropy production measurement is obtained by totaling the conjugated fluxes and the forces developed. The nondimensional local entropy production is given by (Woods [40]) in a convective process and under the effect of the magnetic field as:

$$S_{Gen} = \frac{k_m}{(T_{avg})^2} \left[ \left( \frac{\partial \theta}{\partial X} \right)^2 + \left( \frac{\partial \theta}{\partial Y} \right)^2 \right] + \frac{\mu_{nf}}{T_{avg}} \left[ \frac{\epsilon_p}{K} (U^2 + V^2) + 2 \left( \frac{\partial U}{\partial X} \right)^2 + 2 \left( \frac{\partial V}{\partial Y} \right)^2 + \left( \frac{\partial U}{\partial Y} + \frac{\partial V}{\partial X} \right)^2 \right] + \frac{\sigma_{nf}}{T_{avg}} B^2 V \quad (29)$$

where  $T_{avg} = \frac{T_H + T_C}{2}$ .

### 3.4. Numerical Procedure

It should be noted that the abovementioned governing equations, as well as the boundary conditions, are solved using the finite element method. The equations are solved numerically by the Galerkin weighted residual finite element method. The computational domain is discretized into triangular elements. Triangular Lagrange finite elements of different orders are used for each of the flow variables within the computational domain. Residuals for each conservation equation are obtained by substituting the approximations into the governing equations. To simplify the nonlinear terms in the momentum equations, a Newton–Raphson iteration algorithm was used. The convergence of the solution is assumed when the relative error for each of the variables satisfies the following convergence criteria:

$$\left| \frac{\Gamma^{i+1} - \Gamma^i}{\Gamma^i} \right| \leq \eta$$

where  $i$  represents the iteration number and  $\eta$  is the convergence criterion. In this study, the convergence criterion was set at  $\eta = 10^{-6}$ .

## 4. Validation and Grid Independency Analysis

Five different grids were used to confirm that the results were not dependent on the grid. The  $Nu_{avg}$  and the stream function (shown in Table 2) are used as the indicators of the results. Due to the different results, the fourth grid was preferred as the final grid, ensuring the numerical solution method is one of the primary criteria for achieving results. Previous studies by Calcagni et al. [41] and Ghassemi et al. [42] were used to validate our model, as shown in Figure 3 and Table 3. It should be noted that the streamlines in the upper part of the validation in Figure 3 do not coincide because of the grid size used in the simulated case. We believe that having a finer grid resolves these discrepancies and, also, that the discretization method used is different from the compared case in the literature.

**Table 2.** Evaluation of the mean Nusselt number ( $Nu_{avg}$ ) and  $\psi_{max}$  for diverse grid resolution.

Mesh size	2988	4740	2442	<b>29912</b>	41728
$Nu_{avg}$	7.2360	7.2876	7.4241	<b>7.4959</b>	7.4969
$\psi_{max}$	1.3074	1.3181	1.3244	<b>1.3279</b>	1.3306

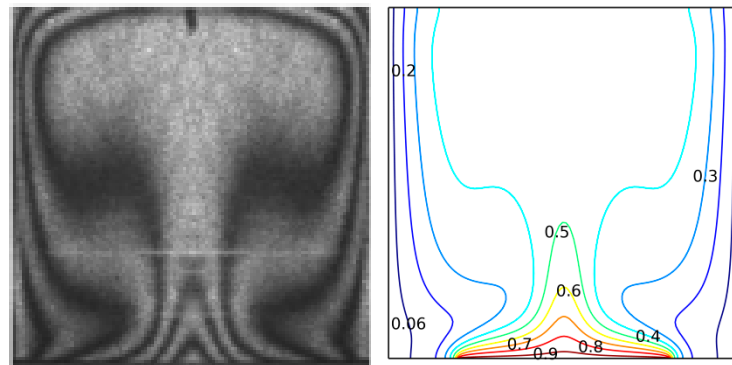


**Figure 3.** (left) Numerical results from Calcagni et al. [35]; (right) The present study for streamlines at Rayleigh number ( $Ra$ ) =  $10^6$ .

**Table 3.** Validation of the present code, for the  $Nu_{avg}$  with  $Ra$  at Hartmann number ( $Ha$ ) = 0, with a cavity by Ghassemi et al. [30].

$Ra$	$10^3$	$10^4$	$10^5$	$10^6$
Present work	1.1803	2.2745	4.8759	9.6335
Ghassemi et al.	1.17612	2.2679	4.8608	9.5918

Moreover, the current code is validated with the case of Fares et al. [5], in which a porous media is included. The cavity considered is a square shape with porous media. Table 4 Shows that the current code gives results with an average error of less than 2% for all the cases compared.

**Table 4.** Validation of the present code, for the entropy generation with Darcy number ( $Da$ ), with a cavity by [5].

	$Da$	$10^{-2}$	$10^{-3}$	$10^{-4}$	$10^{-5}$
Fares et al. [5]	$S_{Gen(max)}$	11.09	7.19	2.01	1.21
Present work		11.0911	7.1897	2.0102	1.1989

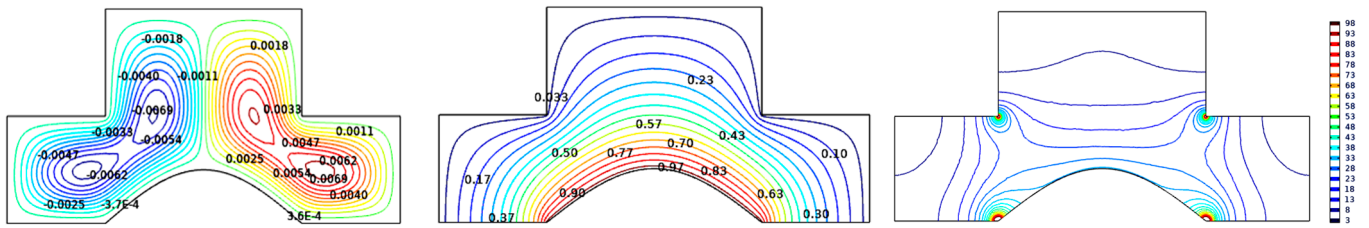
### 5. Results Discussion

In this section, we describe the numerical outcomes for the streamlines, isotherms, and the general entropy concerning five parameters. Those parameters denote Rayleigh number ( $10^3 \leq Ra \leq 10^6$ ), Hartmann number ( $0 \leq Ha \leq 100$ ), nanoparticle volume fraction ( $0 \leq \phi \leq 0.08$ ), and Darcy number ( $10^{-5} \leq Da \leq 10^{-2}$ ), and the porosity is ( $0.2 \leq \epsilon_p \leq 0.8$ ). The base fluid and solids, Ag and AgO, phase thermophysical properties are tabulated in Table 1. According to the governing parameters, the results are classified into four subsections, where, in a particular subsection, we considered the impact of the individual parameter, while the remaining parameters are maintained at constant values.

#### 5.1. Effect of Rayleigh Number

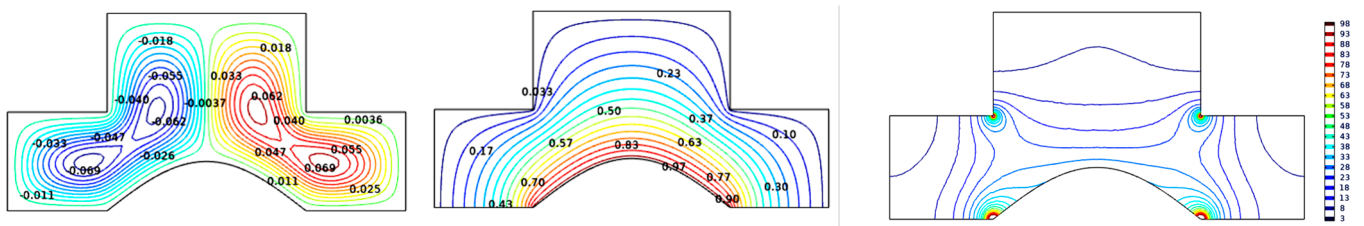
Figure 4 shows the isosurfaces of the governing variables for different magnitudes of the  $Ra$  number at  $Ha = 0$ ,  $Da = 0.01$ ,  $\phi = 0.02$ , and  $\epsilon_p = 0.4$ . The increase in  $Ra$  characterizes a start of the temperature contrast between the hot wall and cooler.

$\psi_{\max} = 0.0067 \quad \psi_{\min} = -0.0067$



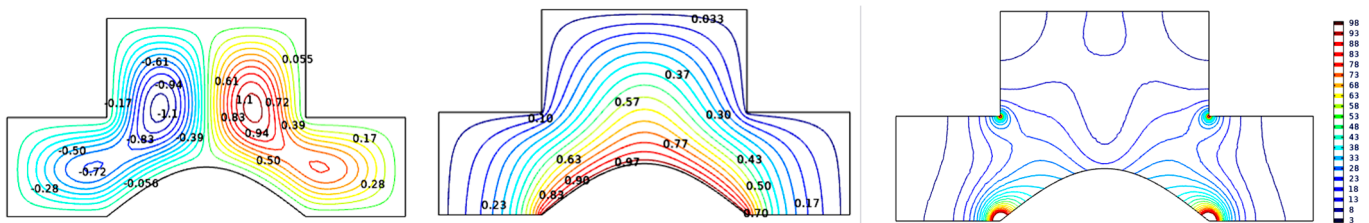
(a)  $Ra = 10^3$

$\psi_{\max} = 0.073 \quad \psi_{\min} = -0.067$



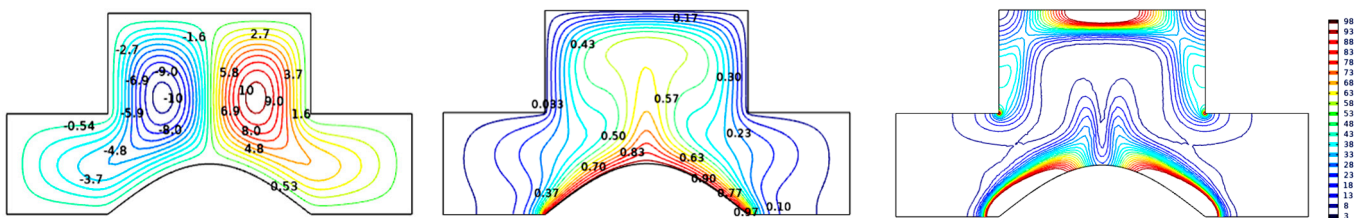
(b)  $Ra = 10^4$

$\psi_{\max} = 1.112 \quad \psi_{\min} = -1.112$



(c)  $Ra = 10^5$

$\psi_{\max} = 10.660 \quad \psi_{\min} = -10.659$



(d)  $Ra = 10^6$

**Figure 4.** Variations of the streamlines (left), isotherms (middle), and general entropy (right) with various values of Rayleigh number ( $Ra$ ), solid volume fraction ( $\phi$ ) = 0.02,  $Ha = 0$ ,  $Da = 0.01$ , nanoparticle volume fraction ( $\phi$ ) = 0.02, and porosity ( $\epsilon_p = 0.4$ ).

The highest value of the stream function increases. This phenomenon means a stronger vortex, and therefore higher velocity of the vortex in the enclosure. The second characteristic is that the density of the streamlines close to the walls, increases.

This means that the temperature gradient enhances close to the walls. Hence, the vortex size increases in this area. The Ra number represents the buoyancy force. An augmentation in the Ra results in an increase in the buoyancy force. The buoyancy force is because of the difference between the density of the cold and hot fluid in the area of the cold and hot walls, respectively. A vortex is created as a result of the fluid movement in the enclosure. The vortex velocity increases by increasing the value of the Ra number, this will lead to an enhancement of heat transfer.

Entropy generation due to heat transfer accumulates around the upper cold wall and increases in the lower-left corner with increasing values of Ra, due to increased kinetic energy and due to a decrease in the velocity near the boundary layer; however, for values of  $Ra \leq 10^4$ , the entropy generation occupied almost the entire cavity. Since thermal entropy production and the entropy production due to fluid friction are small, the isentropic lines are slightly similar to each other.

In Figures 5–10, the values of Nu calculated on the hot wall, Nusselt average, and total entropy are displayed for different values of Ra, Ha, Da,  $\phi$ , and  $\varepsilon_p$ .

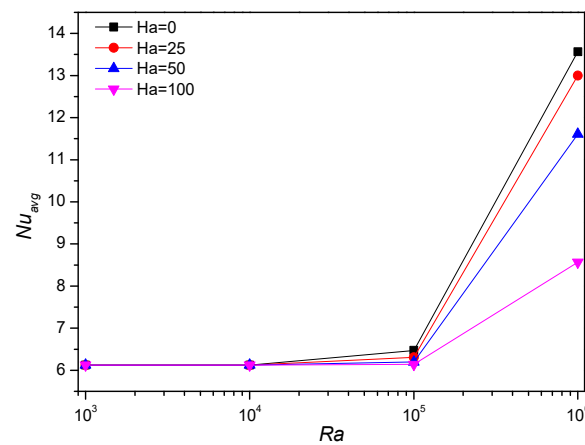


**Figure 5.** Average Nusselt number ( $Nu_{ave}$ ) as a function of Rayleigh number (Ra) at various values of Hartmann number (Ha).  $Da = 0.01$ ,  $\phi = 0.02$ , and  $\varepsilon_p = 0.4$ .

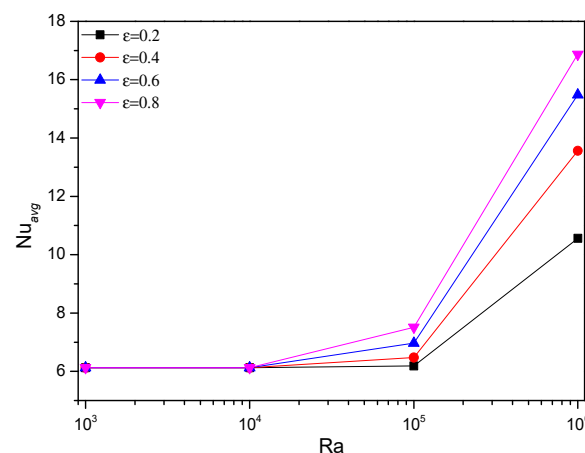


**Figure 6.** Average Nusselt number ( $Nu_{ave}$ ) as a function of Rayleigh number (Ra) at various values of porosity ( $\varepsilon_p$ ).  $Ha = 0$ ,  $Da = 0.01$  and  $\phi = 0.02$ .

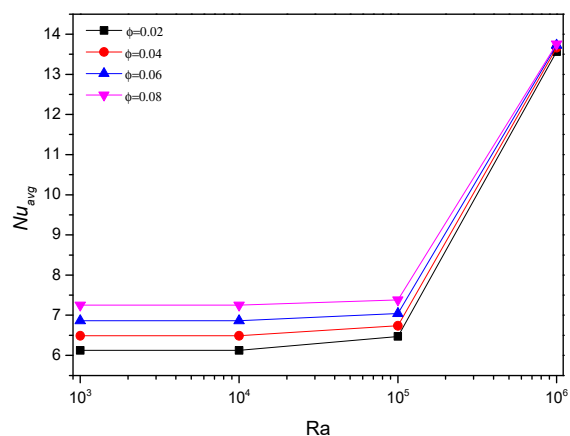


**Figure 7.** Average Nusselt number ( $Nu_{ave}$ ) as a function of Rayleigh number ( $Ra$ ) at various values of solid volume fraction ( $\phi$ ).  $Ha = 0$ ,  $Da = 0.01$  and  $\epsilon_p = 0.4$ .

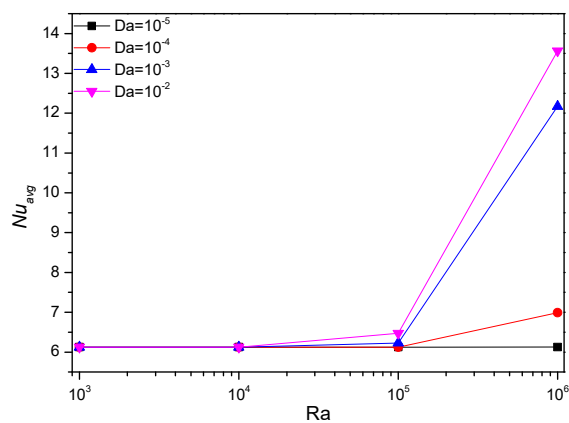


**Figure 8.** Average Nusselt number ( $Nu_{ave}$ ) as a function of Rayleigh number ( $Ra$ ) at various values of Darcy number ( $Da$ ).  $\phi = 0.02$  and  $\epsilon_p = 0.4$ .

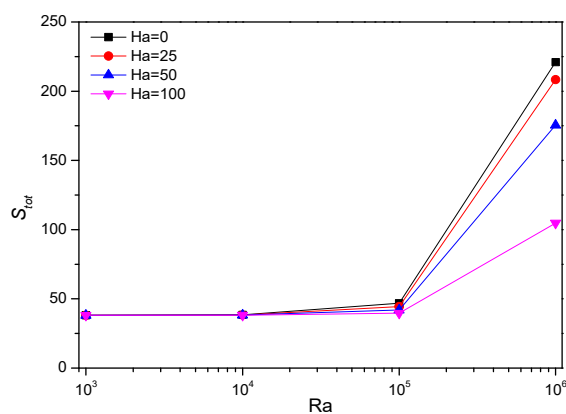


**Figure 9.** Total entropy as a function of Rayleigh number ( $Ra$ ) at various values of Hartmann number ( $Ha$ ).  $Da = 0.01$ ,  $\phi = 0.02$  and  $\epsilon_p = 0.4$ .

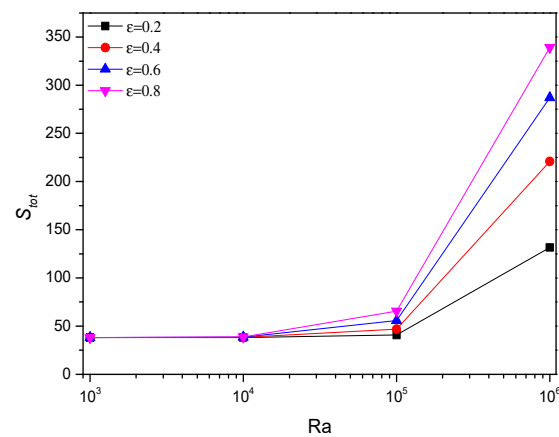


**Figure 10.** Total entropy as a function of Rayleigh number (Ra) at various values of porosity ( $\epsilon_p$ ).  $Ha = 0$ ,  $Da = 0.01$  and  $\phi = 0.02$ .

Figure 5 reveals that the  $Nu_{avg}$  increases with the Ra, this process is detected for all values of Ha. This is because an augmentation in the buoyancy force by enhancing the Ra results in an augmentation in the velocity of the fluid in the enclosure, hence, the Nu decreases. The  $Nu_{avg}$  diminishes with the Ha and the Lorentz force. This is due to the fact that Lorentz force prevents the formation of vortices, which leads to a reduction in the velocity of the fluid in the cavity, resulting in a reduction in the Nu.

Variation of  $Nu_{avg}$  with Ra for different  $\epsilon_p$  values is presented in Figure 6. The  $Nu_{avg}$  increases with Ra for all values of  $\epsilon_p$ . Additionally, increasing  $\epsilon$  enhances Nu and heat transfer for higher values of Ra, as fluid motion (and hence convective heat transfer) is hindered for low porosities. The effect is not seen for low values of Ra due to conductive heat transfer dominance. It should be mentioned that the enhancement is most evident when increasing  $\epsilon$  in the small ranges (e.g., 26% enhancement with an increase from  $\epsilon_p = 0.2$  to  $\epsilon_p = 0.4$  at  $Ra = 10^6$  as compared with the enhancement of 10% with an increase from  $\epsilon_p = 0.6$  to  $\epsilon_p = 0.8$  for the same Ra). Therefore, the improvement of fluid motion is also more significant in the lower ranges.

Figure 7 demonstrates the variation of  $Nu_{avg}$  with Ra for different values of the volume fraction of the nano-solid particles ( $\phi$ ). For Ra values below 100,000, values of  $Nu_{avg}$  are almost equal with increasing values of Ra, besides increasing  $\phi$  does not significantly increase Nu. The almost equal behavior is due to the equilibrium between conduction and convection. The highest heat transfer rate occurs with the upper values of Ra, and we notice the disappearance of any difference of Cloud for different  $\phi$ .

To further examine the effect of permeability and its relation to the cross-sectional area in the problem, the  $Nu_{avg}$  change with Ra at different values of Da is shown in Figure 8. The plots and conclusions are identical to those in Figure 6, where more fluid freedom of motion represents better heat transfer, which is attributed to better convection.

Variations of total entropy generation with various values of Ra for Ha are shown in Figure 9. The entropy generation increases with Ra for higher Ra values regardless of Ha. However, and projecting it to Figure 5, it can be seen that for high values of Ra, the vortices and heat transfer decrease with increased Ha, and the Lorentz force is also accompanied by a decrease in the total entropy. This reflects the superior role of the thermal and fluid friction entropy as compared with the entropy, due to the magnetic field for that Ra range. For the small Ra range, the thermal and fluid friction entropy generation is small, reducing the total entropy generation, and therefore the Ha has no impact.

Figure 10 represents variations of total entropy generated with various values of Ra for different  $\epsilon_p$ , and the results are similar to those in Figure 6. That means, the entropy generation (as mentioned upward) is governed mainly by thermal and fluid friction entropy generation (large heat transfer from more freedom of fluid motion) at high values of Ra, whereas at low values of Ra the entropy generation is indifferent to various  $\epsilon_p$  values.

The total entropy generation, plotted against Ra for different  $\phi$  values, is plotted in Figure 11. Clearly, the variation of  $\phi$  does not impact total entropy generation significantly, which, once again, confirms that the total entropy generation is mainly governed by heat transfer, and heat transfer has shown small variations with different  $\phi$  values given in Figure 7.

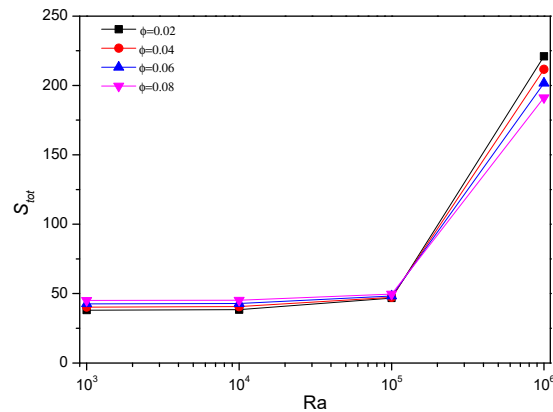


**Figure 11.** Total entropy as a function of Rayleigh number (Ra) at various values of solid volume fraction ( $\phi$ ).  $Ha = 0$ ,  $Da = 0.01$  and  $\varepsilon_p = 0.4$ .

Figure 12, which plots the total entropy generation against Ra for different Da numbers, can be compared again with Figure 8 to realize the dominance of the thermal and fluid motion (friction) contribution to the total entropy generation.

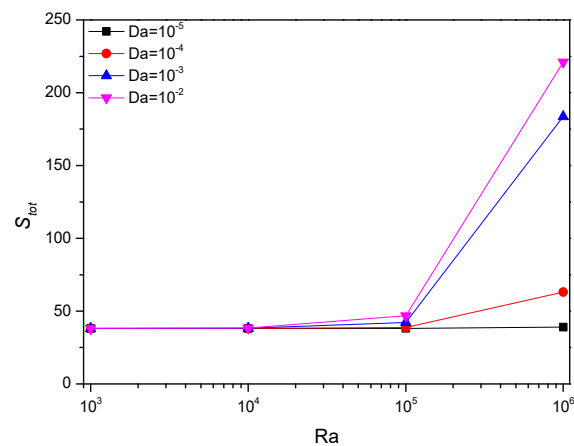


**Figure 12.** Total entropy as a function of Rayleigh number (Ra) at various values of Darcy number (Da).  $Ha = 0$ ,  $\phi = 0.02$  and  $\varepsilon_p = 0.4$ .

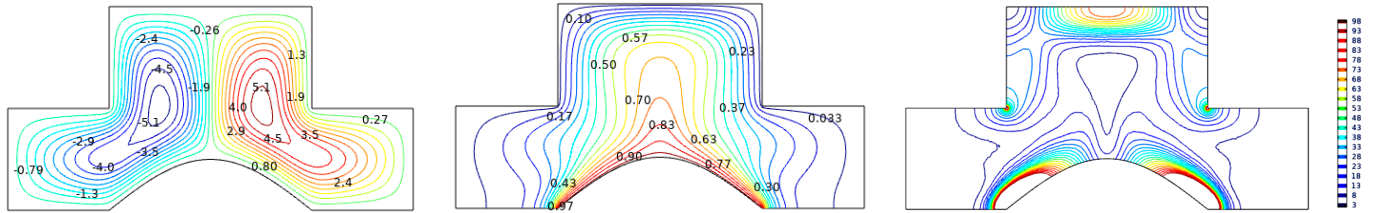
Therefore, the main conclusion from Figures 9–12 is that whenever a parameter enhances heat transfer, total entropy generation is impacted in a similar manner (increase), as the thermal entropy generation contribution clearly is dominant against other entropy generation components, especially for high values of Ra.

### 5.2. Effect of Nanofluid Loading

Figures 13–15 characterize the influence of the solid volume fraction. A growth of  $\phi$  characterizes a weak modification of streamlines and isotherms, while isoconcentrations are modified significantly. A solid volume fraction increment characterizes an increase in the entropy plume adjacent to the top of the cavity. Other changes are insignificant. Figures relating to the local Nusselt number and total entropy versus  $\phi$  are shown in Figures 14 and 15 at  $Ra = 10^6$  and  $Da = 0.01$ , and different  $\varepsilon_p$ . A solid volume fraction reflects the

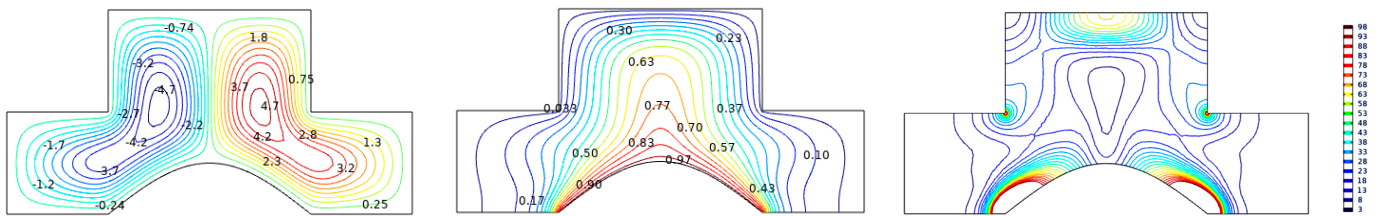
temperature gradient increase along the heater zone. It should be noted that the negative values about Nu correspond to the upper part of the cylinder where the cylinder is heated from the hot temperature wave, while the positive magnitudes correspond to the bottom part of the cylinder where the cylinder heats the surrounding liquid.

$$\psi_{\max} = 5.336 \quad \psi_{\min} = -5.336$$



(a)  $\phi = 0.02$

$$\psi_{\max} = 5.003 \quad \psi_{\min} = -5.003$$



(b)  $\phi = 0.08$

**Figure 13.** Variations of the streamlines (left), isotherms (middle), and entropy generation (right) with various solid volume fraction ( $\phi$ ) at  $Ra = 10^6$ ,  $Ha = 50$ ,  $\varepsilon = 0.4$ , and  $Da = 0.01$ .

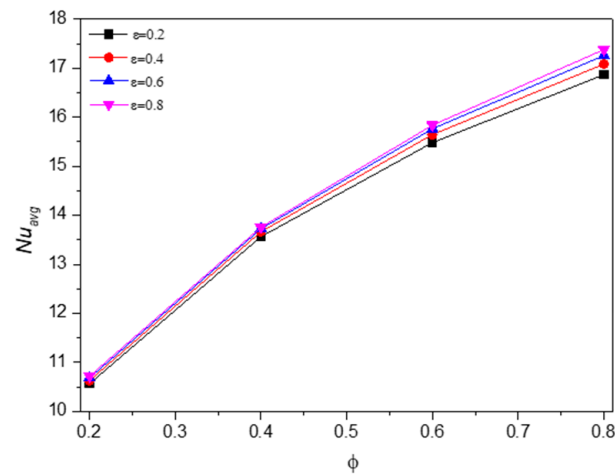


**Figure 14.** Average Nusselt number ( $Nu_{ave}$ ) as a function of solid volume fraction ( $\phi$ ) at various values of porosity  $\varepsilon_p$ .  $Ra = 10^6$ ,  $Ha = 0$ , and  $Da = 0.01$ .

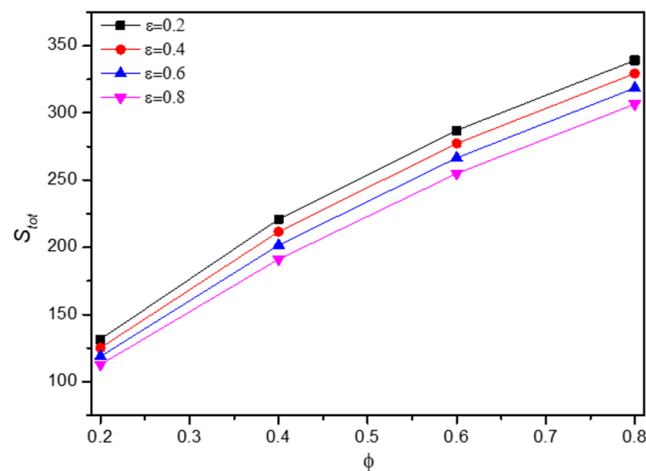


**Figure 15.** Total entropy as a function of solid volume fraction ( $\phi$ ) at various values of porosity  $\epsilon_p$ .  $Ra = 10^6$ ,  $Ha = 0$ , and  $Da = 0.01$ .

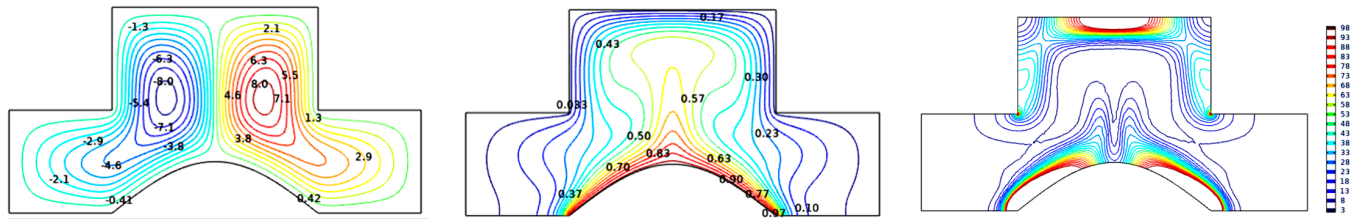
Figure 14 reveals the role of increasing  $\phi$  on heat transfer, and thus the increase in entropy, shown in Figure 15. On the contrary, the impact of varying  $\epsilon_p$  is insignificant (the maximum is less than 3% for  $Nu$  and 11% for entropy, both are occurring at the highest  $\phi$ ).

### 5.3. Effect of Hartmann Number

Hartmann number is a direct indication of the amount of electromagnetic loading impacting the nanofluid. To investigate its impact, the streamlines, isotherms, and entropy generations were plotted for various  $Ha$ , ranging from 0 to 100 (Figure 16). First, symmetry about the vertical centerline is apparent in all cases of  $Ha$ . Nonetheless, comparing case to case, it can be clearly seen that  $Ha$  extensively changes all the aforementioned; especially for  $Ha$  values higher than 25. That is, while there is a similarity between a zero magnetic field and a small magnetic field, once the electromagnetic force becomes dominant as compared with the viscous force, the changes are clearly observed. For the streamlines, the plume centers are pushed downward under the effect of the Lorentz force, bringing vortex centers closer to the hot surface, but much slower ( $\sim 64\%$  drop in the velocity of the center of  $Ha = 0$  to  $Ha = 100$ ), which, in turn, impacts the isothermal lines by making them more uniform (closer to stagnant fluid heat conduction), with diminished “thermal void/jump” in the center of the upper part. The result is a much-smoothed thermal gradient which reduces heat transfer. Consequently, the entropy generation, especially near the center of the top, is impacted.

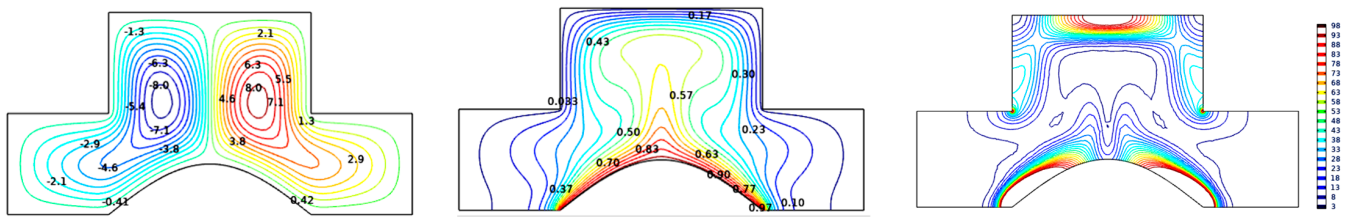
Figures 17–20 provide more insight about the variation of  $Ha$  at the higher  $Ra$  value of  $10^6$  and with  $Da = 0.01$ . The general conclusion, which was previously drawn earlier, that increasing the value of  $Ha$  will dampen the heat transfer, and thus the entropy generation is still applicable. However, it is of interest to know that varying the nano-solid particles volume fraction  $\phi$  between 0.02 and 0.08 is not impacting the heat transfer for such  $Ra$  and  $Da$  at all  $Ha$  values (evidenced by Figure 17). In addition, the entropy generation is minimally affected by  $\phi$ , where the greatest is at low  $Ha$  values, and disappears with higher  $Ha$  (Figure 18). Contrary to  $\phi$ , the porosity ( $\epsilon_p$ ) (Figures 19 and 20) affects the heat transfer and total entropy, as concluded before from Figures 6 and 10, respectively. Nonetheless, the new revelation here is the dampening effect of the  $Ha$  on the improvement  $\epsilon_p$  on both  $Nu$  and entropy. In a summary, the main conclusion drawn from these figures is that at high values of  $Ra$  where heat transfer is usually governed by convection and fluid motion and vortices, and hence generation of large amounts of entropy, all of that can be damped down by increasing the magnetic field which, in turn, reduces the motion of the fluid, and hence reduces the efficiency of the heat transfer.

$\psi_{\max} = 10.660 \quad \psi_{\min} = -10.659$



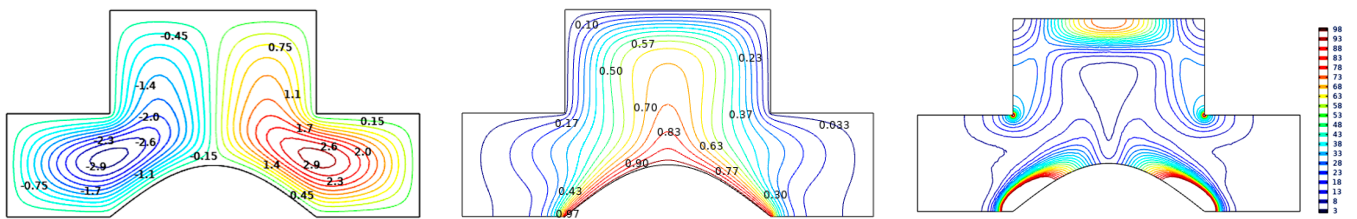
(a)  $Ha=0$

$\psi_{\max} = 8.391 \quad \psi_{\min} = -8.393$



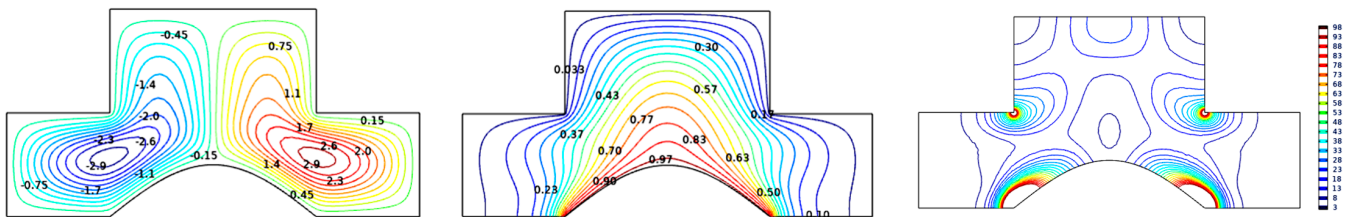
(b)  $Ha=25$

$\psi_{\max} = 5.536 \quad \psi_{\min} = -5.536$



(c)  $Ha=50$

$\psi_{\max} = 3.019 \quad \psi_{\min} = -3.019$



(d)  $Ha=100$

**Figure 16.** Variations of the streamlines (left), isotherms (middle), and general entropy (right) with various values of Hartmann number ( $Ha$ ).  $\phi = 0.02$ ,  $Ra = 10^6$ ,  $Da = 0.01$ , and  $\varepsilon = 0.4$ .

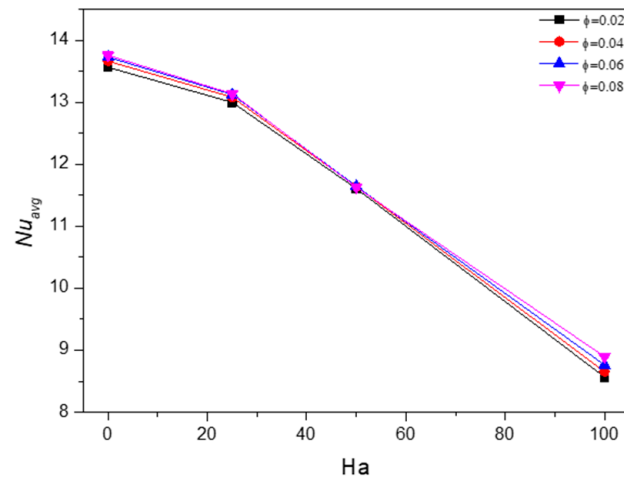


**Figure 17.** Average Nusselt number ( $Nu_{ave}$ ) as a function of Hartmann number ( $Ha$ ) at various values of  $\phi$ .  $Ra = 10^6$ ,  $Da = 0.01$ , and  $\epsilon_p = 0.4$ .

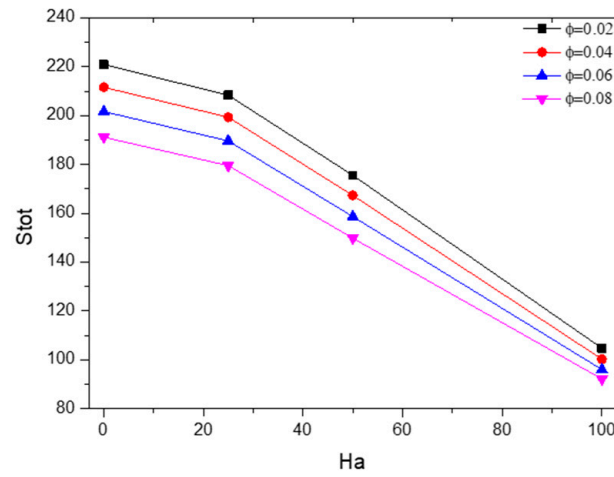


**Figure 18.** Total entropy as a function of Hartmann number ( $Ha$ ) for various values of  $\phi$ .  $Ra = 10^6$ ,  $Da = 0.01$ , and  $\epsilon_p = 0.4$ .

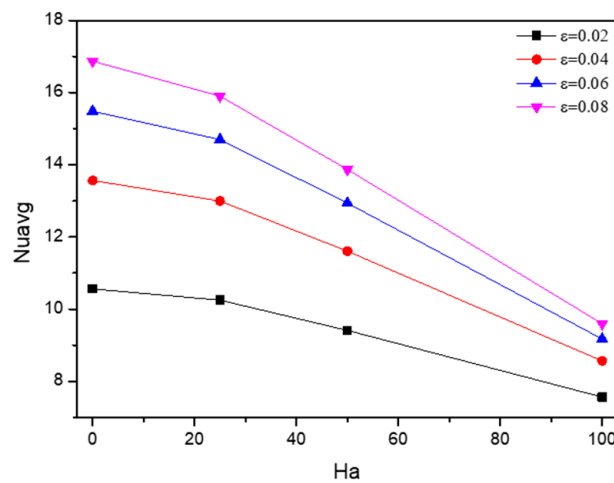


**Figure 19.** Average Nusselt number ( $Nu_{ave}$ ) as a function of Hartmann number ( $Ha$ ) at various values of porosity  $\epsilon_p$ .  $Ra = 10^6$ ,  $\phi = 0.02$ , and  $Da = 0.01$ .

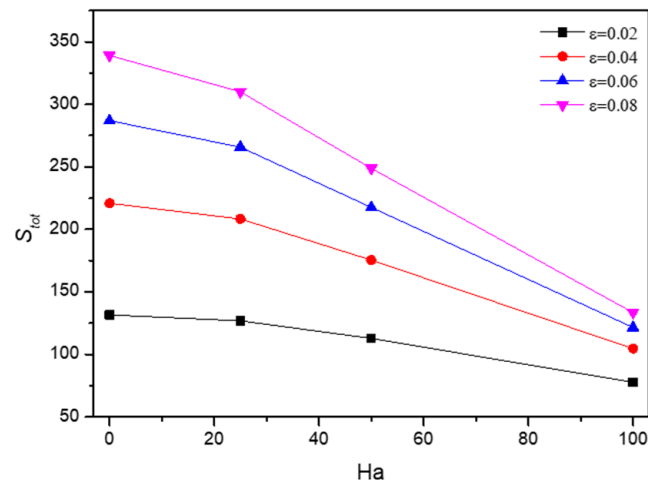


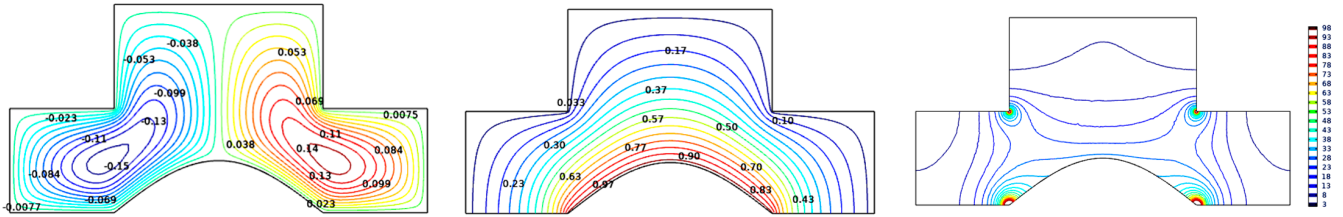
**Figure 20.** Total entropy as a function of Hartmann number (Ha) at various values of porosity  $\epsilon_p$ .  $Ra = 10^6$ ,  $\phi = 0.02$ , and  $Da = 0.01$ .

#### 5.4. Effect of Darcy Number

Darcy number is an indicator of how easy the fluid is allowed to flow within the medium characterized by the permeability of the medium through which the fluid flows with respect to its cross-section. Figure 21 investigates that at  $\phi = 0.02$ ,  $Ra = 10^6$ ,  $Ha = 0$  and  $\epsilon_p = 0.4$  by providing visualization of the streamlines, isotherms, and entropy. For a high Da number (last row of the figure,  $Da = 0.01$ ), permeability is granted to the fluid rendering the vortices in the middle of the cross-section between the lower hot surface and the upper cold surface and with high velocity. However, decreasing the Da reveals attempts of the medium to stagnate or resist at least the fluid motion, and vortices are pushed downward in the direction of gravity. The former is accompanied by an enhanced heat transfer evidenced by the jump in the thermo lines, where the latter shows smoothed uniform temperature gradient revealing decreased heat transfer. Thus, entropy follows as explained earlier due to the dominance of the thermal entropy.

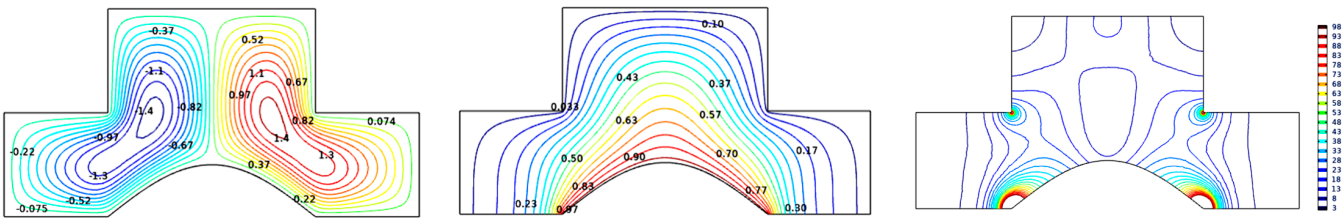
Figures 22 and 23 study Nu and total entropy values at variations of Da and  $\epsilon_p$  at the a high value of Ra. Not surprisingly, increasing  $\epsilon_p$  and Da work, hand in hand, providing more freedom of fluid motion and enhancing convective heat transfer, and thus the total entropy. Finally, Figures 24 and 25 show that the role of  $\phi$  on Nu and total entropy is not significant, especially for high values of Da for Nu and low values of Da for  $S_{tot}$ . Still, it is of interest that Figure 25 shows the flipping behavior for different values of  $\phi$  across the Da range. For example, at low values of Da, the largest  $\phi$  is marginally the dominant, where at high values of Da, the smallest  $\phi$  is marginally dominant. Physically, that can be attributed to the fact that, on the one hand, high values of Da enhance permeability for nanoparticles up to a certain size, giving them more movement, more heat transfer, and producing more entropy. On the other hand, at low values of Da, almost all nanoparticle sizes are hindered, and those with more size create marginally more entropy in the fluid friction. All in all, increased values of Da will always provide higher Nu, due to permissible fluid motion, and hence increase generated entropy.

$\psi_{\max} = 0.151 \quad \psi_{\min} = -0.151$



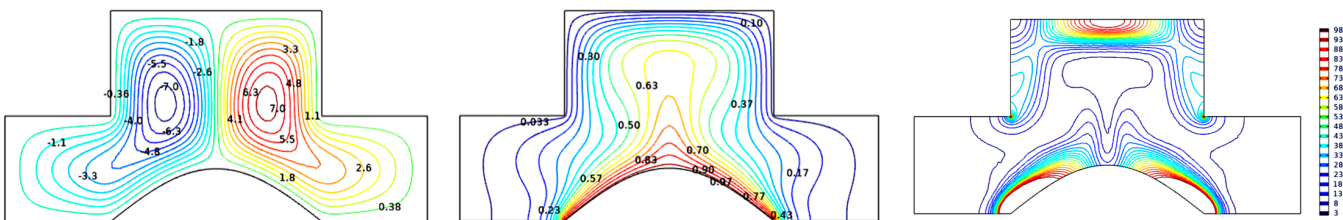
(a)  $Da = 10^{-5}$

$\psi_{\max} = 1.487 \quad \psi_{\min} = -1.486$



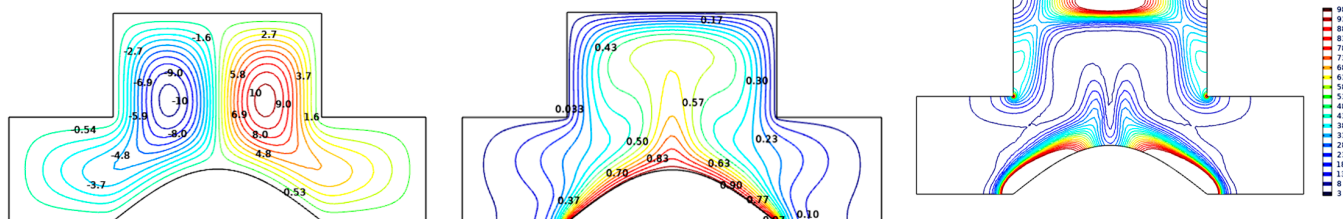
(b)  $Da = 10^{-4}$

$\psi_{\max} = 7.378 \quad \psi_{\min} = -7.378$



(c)  $Da = 10^{-3}$

$\psi_{\max} = 10.660 \quad \psi_{\min} = -10.659$



(d)  $Da = 10^{-2}$

**Figure 21.** Variations of the streamlines (left), isotherms (middle), and general entropy (right) with various values of Darcy number (Da).  $\phi = 0.02$ ,  $Ra=10^6$ ,  $Ha= 0$ , and  $\varepsilon = 0.4$ .

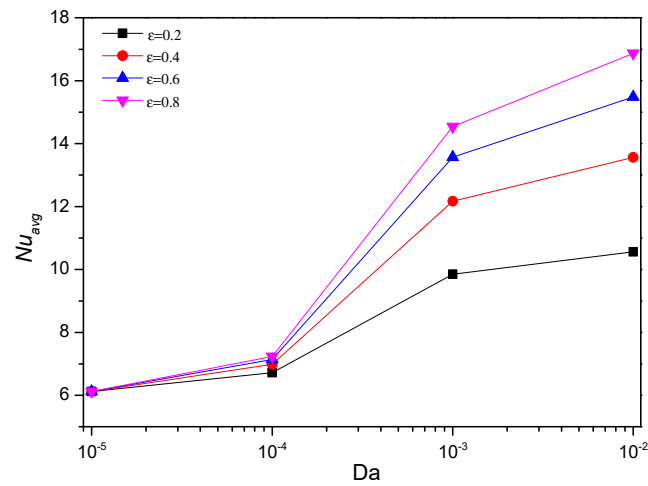


**Figure 22.** Average Nusselt number ( $Nu_{avg}$ ) as a function of Darcy number ( $Da$ ) at various values of  $\epsilon$ .  $Ra = 10^6$ ,  $\phi = 0.02$  and  $Ha = 0$ .

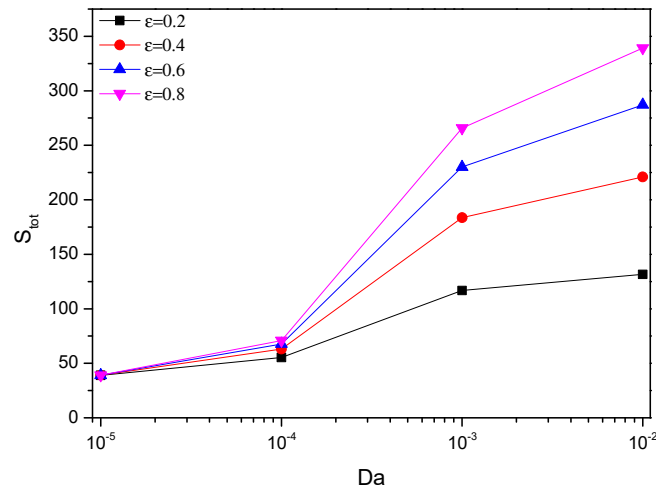


**Figure 23.** Total entropy as a function of Darcy number ( $Da$ ) at various values of  $\epsilon$ .  $Ra = 10^6$ ,  $\phi = 0.02$  and  $Ha = 0$ .

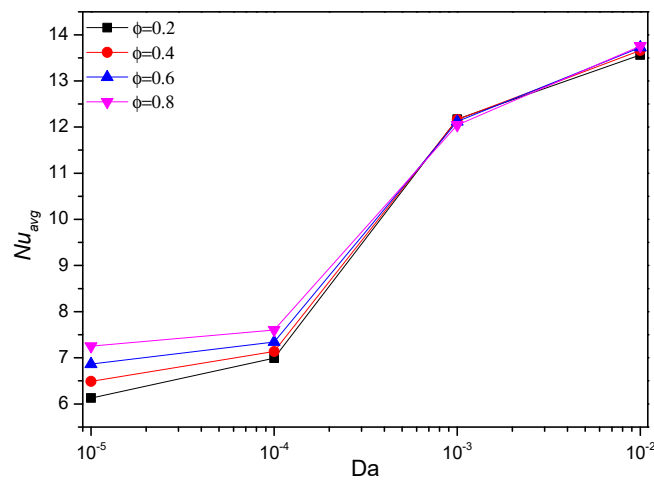


**Figure 24.** Average Nusselt number ( $Nu_{avg}$ ) as a function of Darcy number ( $Da$ ) at various values of  $\phi$ .  $Ra = 10^6$ ,  $\epsilon = 0.4$  and  $Ha = 0$ .

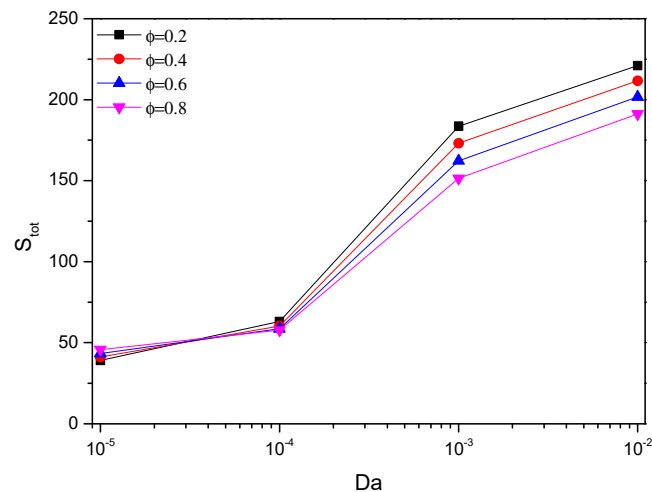


**Figure 25.** Total entropy as a function of Darcy number (Da) at various values of  $\phi$ .  $Ra = 10^6$ ,  $\varepsilon = 0.4$  and  $Ha = 0$ .

## 6. Conclusions

The finite element method is used to study a new cavity form filled under a constant magnetic field by Ag/MgO/water nanofluids and porous media. The streamlines, natural convection, and total entropy were examined for various parameter effects. The main conclusion revealed that any parameter that increases is responsible for limiting the motion of the fluid, and therefore directly limits the effective heat transfer and the total entropy generation. The  $Ha$  and  $Da$  are examples of these parameters. In contrast,  $\varepsilon_p$  improves heat transfer. Some other factors were shown to marginally affect heat transfer such as the volume fraction of the nano-solid particles, especially for high values of  $Ra$ . The thermal entropy generation has also been shown to dominate the other entropy components. Finally, understanding the impacts of all of these parameters has direct application for implementing an elaborate heat transfer. The heat transfer can even be controlled through the variation of the magnetic field, especially for high values of  $Ra$ .

**Author Contributions:** Conceptualization and writing—original draft preparation, N.A.-L., F.R., A.A. (Ahmad Almuhtady), A.A. (Abderrahmane Aissa), W.A.-K.; validation, writing—review and editing, W.J., A.A. (Abderrahmane Aissa), A.A. (Ahmad Almuhtady), F.M.-O.; software, F.R., A.A. (Abderrahmane Aissa); supervision, N.A.-L., W.A.-K., F.M.-O., F.R. All authors have read and agreed to the published version of the manuscript.

**Funding:** This research received no external funding.

**Institutional Review Board Statement:** Not applicable.

**Informed Consent Statement:** Not applicable.

**Data Availability Statement:** Not applicable.

**Conflicts of Interest:** The authors declare no conflict of interest.

## Abbreviations

### List of symbols

$k$	Thermal conductivity ( $W/m \cdot k$ )
$L, H$	Long and height of the cavity (m)
$l_1, l_2$	Long and height of heat wall (m)
$Ra$	Rayleigh number
$Ha$	Hartmann number
$Nu$	Nusselt number
$Nu_{avg}$	Average Nusselt number

$Nu_{loc}$	Local Nusselt number
Pr	Prandtl number
Da	Darcy number
$x, y$	Coordinate(m)
$X, Y$	Dimensionless coordinate
$u, v$	Velocity components(m/s)
$U, V$	Nondimensional velocity components
$T$	Temperature ( $^{\circ}\text{C}$ )
$p$	Pressure ( $\text{N}/\text{m}^2$ )
$P$	Dimensionless pressure
$K$	Permeability
$g$	Gravitational acceleration vector ( $\text{m}/\text{s}^2$ )
$F_c$	Forchheimer coefficient
$B_0$	Intensity of magnetic field
$S_{Gen}$	Total dimensionless entropy generation
<b>Greeks symbols</b>	
$\theta$	Dimensionless temperature
$\varepsilon_p$	Porosity
$\alpha$	Thermal diffusivity ( $\text{m}^2/\text{s}$ )
$\nu$	Kinematic viscosity ( $\text{m}^2/\text{s}$ )
$\phi$	Volume fraction
$\beta$	Thermal expansion coefficient ( $1/\text{K}$ )
$\mu$	Dynamic viscosity ( $\text{kg}/\text{m}\cdot\text{s}$ )
$\rho$	Density ( $\text{kg}/\text{m}^3$ )
$\sigma$	Electrical conductivity ( $\Omega\cdot\text{m}$ ) <sup>-1</sup>
$\psi$	Nondimensional stream function
<b>Subscripts</b>	
$bf$	Base fluid
$hnf$	Hybrid-nanofluid
$np$	Nanoparticles
$avg$	Average
$loc$	Local
$h$	Hot
$c$	Cold

## References

- Choi, S.U.S.; Eastman, J.A. *Enhancing Thermal Conductivity of Fluids with Nanoparticles*; Argonne National Lab.: Lemont, IL, USA, 1995.
- Maxwell, J.C. *Electricity and Magnetism*; Clarendon Press: Oxford, UK, 1873.
- Diglio, G.; Roselli, C.; Sasso, M.; Channabasappa, U.J. Borehole heat exchanger with nanofluids as heat carrier. *Geothermics* **2018**, *72*, 112–123. [[CrossRef](#)]
- Zaim, A.; Aissa, A.; Mebarek-Oudina, F.; Mahanthesh, B.; Lorenzini, G.; Sahnoun, M.; El Ganaoui, M. Galerkin finite element analysis of magneto-hydrodynamic natural convection of Cu-water nanoliquid in a baffled U-shaped enclosure. *Propuls. Power Res.* **2020**, *9*, 383–393. [[CrossRef](#)]
- Fares, R.; Mebarek-Oudina, F.; Aissa, A.; Bilal, S.M.; Öztop, H.F. Optimal Entropy Generation in Darcy-Forchheimer Magnetized Flow in a Square Enclosure Filled with Silver Based Water Nanoliquid. *J. Therm. Anal. Calorim.* **2021**, 1–11. [[CrossRef](#)]
- Mebarek-Oudina, F.; Redouane, F.; Rajashekhar, C. Convection Heat Transfer of MgO-Ag/Water Magneto-Hybrid Nanoliquid Flow into a Special Porous Enclosure. *Alger. J. Renew. Energy Sustain. Dev.* **2020**, *2*, 84–95. [[CrossRef](#)]
- Molana, M. A Comprehensive Review on the Nanofluids Application in the Tubular Heat Exchangers. *Am. J. Heat Mass Transf.* **2016**, *3*, 352–381. [[CrossRef](#)]
- Sui, D.; Langåker, V.H.; Yu, Z. Investigation of Thermophysical Properties of Nanofluids for Application in Geothermal Energy. *Energy Procedia* **2017**, *105*, 5055–5060. [[CrossRef](#)]
- Chamkha, A.J.; Molana, M.; Rahnama, A.; Ghadami, F. On the nanofluids applications in microchannels: A comprehensive review. *Powder Technol.* **2018**, *332*, 287–322.
- Patterson, J.; Imberger, J. Unsteady natural convection in a rectangular cavity. *J. Fluid Mech.* **1980**, *100*, 65–86. [[CrossRef](#)]
- Armaghani, T.; Kasaeipoor, A.; Alavi, N.; Rashidi, M.M. Numerical investigation of water-alumina nanofluid natural convection heat transfer and entropy generation in a baffled L-shaped cavity. *J. Mol. Liq.* **2016**, *223*, 243–251. [[CrossRef](#)]

12. Malekpour, A.; Karimi, N.; Mehdizadeh, A. Magnetohydrodynamics, natural convection and entropy generation of CuO-water nanofluid in an I-shape enclosure. *J. Therm. Sci. Eng. Appl.* **2018**, *10*, 061016. [[CrossRef](#)]
13. Mamourian, M.; Shirvan, K.M.; Pop, I. Sensitivity analysis for MHD effects and inclination angles on natural convection heat transfer and entropy generation of Al<sub>2</sub>O<sub>3</sub>-water nanofluid in square cavity by Response Surface Methodology. *Int. Commun. Heat Mass Transf.* **2016**, *79*, 46–57. [[CrossRef](#)]
14. Bondareva, N.S.; Sheremet, M.A.; Oztop, H.F.; Abu-Hamdeh, N. Heatline visualization of MHD natural convection in an inclined wavy open porous cavity filled with a nanofluid with a local heater. *Int. J. Heat Mass Transf.* **2016**, *99*, 872–881. [[CrossRef](#)]
15. Dogonchi, A.S.; Armaghani, T.; Chamkha, A.J.; Ganji, D.D. Natural Convection Analysis in a Cavity with an Inclined Elliptical Heater Subject to Shape Factor of Nanoparticles and Magnetic Field. *Arab. J. Sci. Eng.* **2019**, *44*, 7919–7931. [[CrossRef](#)]
16. Rashad, A.M.; Armaghani, T.; Chamkha, A.J.; Mansour, M.A. Entropy generation and MHD natural convection of a nanofluid in an inclined square porous cavity: Effects of a heat sink and source size and location. *Chin. J. Phys.* **2018**, *56*, 193–211. [[CrossRef](#)]
17. Sajjadi, H.; Delouei, A.A.; Izadi, M.; Mohebbi, R. Investigation of MHD natural convection in a porous media by double MRT lattice Boltzmann method utilizing MWCNT-Fe<sub>3</sub>O<sub>4</sub>/water hybrid nanofluid. *Int. J. Heat Mass Transf.* **2019**, *132*, 1087–1104. [[CrossRef](#)]
18. Dogonchi, A.S.; Seyyedi, S.M.; Hashemi-Tilehnoee, M.; Chamkha, A.J.; Ganji, D.D. Investigation of natural convection of magnetic nanofluid in an enclosure with a porous medium considering Brownian motion. *Case Stud. Therm. Eng.* **2019**, *14*, 100502.
19. Mebarek-Oudina, F.; Aissa, A.; Mahanthesh, B.; Öztop, H.F. Heat Transport of Magnetized Newtonian Nanoliquids in an Annular Space between Porous Vertical Cylinders with Discrete Heat Source. *Int. Commun. Heat Mass Transf.* **2020**, *117*, 104737. [[CrossRef](#)]
20. Zahri, M.; Al-Kouz, W.; Rehman, K.U.; Malik, M. Thermally magnetized rectangular chamber optimization (TMRCO) of partially heated continuous stream: Hybrid meshed case study. *Case Stud. Therm. Eng.* **2020**, *22*, 100770. [[CrossRef](#)]
21. Mahanthesh, B.; Mackolil, J.; Radhika, M.; Al-Kouz, W. Significance of quadratic thermal radiation and quadratic convection on boundary layer two-phase flow of a dusty nanoliquid past a vertical plate. *Int. Commun. Heat Mass Transf.* **2021**, *120*, 105029. [[CrossRef](#)]
22. Mukhtar, T.; Jamshed, W.; Aziz, A.; Al-Kouz, W. Computational investigation of heat transfer in a flow subjected to magnetohydrodynamic of Maxwellnanofluid over a stretched flat sheet with thermal radiation. *Numer. Methods Partial. Differ. Equ.* **2020**, 1–21. [[CrossRef](#)]
23. Alshare, A.; Al-Kouz, W.; Alkhalidi, A.; Kiwan, S.; Chamkha, A. Periodically fully developed nanofluid transport through a wavy module. *J. Therm. Anal. Calorim.* **2020**, 1–13. [[CrossRef](#)]
24. Xiong, Q.; Abohamzeh, E.; Ali, J.A.; Hamad, S.M.; Tlili, I.; Shafee, A.; Habibeh, H.; Nguyen, T.K. Influences of nanoparticles with various shapes on MHD flow inside wavy porous space in appearance of radiation. *J. Mol. Liq.* **2019**, *292*, 111386. [[CrossRef](#)]
25. Radouane, F.; Abderrahmane, A.; Mebarek-Oudina, F.; Ahmed, W.; Rashad, A.M.; Sahnoun, M.; Ali, H.M. Magneto-Free Convective of Hybrid Nanofluid inside Non-Darcy Porous Enclosure Containing an Adiabatic Rotating Cylinder. *Energy Sources Part A Recovery Util. Environ. Eff.* **2020**. [[CrossRef](#)]
26. Marzougui, S.; Bouabid, M.; Mebarek-Oudina, F.; Abu-Hamdeh, N.; Magherbi, M.; Ramesh, K. A computational analysis of heat transport irreversibility phenomenon in a magnetized porous channel. *Int. J. Numer. Methods Heat Fluid Flow* **2020**. ahead of print. [[CrossRef](#)]
27. Abo-Dahab, S.M.; Abdelhafez, M.A.; Mebarek-Oudina, F.; Bilal, S.M. MHD Cassonnanofluid flow over nonlinearly heated porous medium in presence of extending surface effect with suction/injection. *Indian J. Phys.* **2021**, 1–15. [[CrossRef](#)]
28. Swain, K.; Mebarek-Oudina, F.; Abo-Dahab, S.M. Influence of MWCNT/Fe<sub>3</sub>O<sub>4</sub> hybrid nanoparticles on an exponentially porous shrinking sheet with chemical reaction and slip boundary conditions. *J. Therm. Anal. Calorim.* **2021**, 1–10. [[CrossRef](#)]
29. Fares, R.; Abderrahmane, A.; Meddeber, A.; Abdelkrim, A. Numerical investigation of hydrodynamic nanofluid convective flow in a porous enclosure. *Nat. Technol.* **2018**, *18*, 54–57.
30. Fares, R.; Naim, H.; Abderrahmane, A.; Bouadi, A. Mixed Convection of Nanofluid Flow in a Vented Cavity Under The Influence Of Magnetic Field. *J. Mater. Struct.* **2020**, *4*, 1–11.
31. Al-Kouz, W.; Saleem, K.B.; Chamkha, A. Numerical investigation of rarefied gaseous flows in an oblique wavy sided walls square cavity. *Int. Commun. Heat Mass Transfer* **2020**, *116*, 104719. [[CrossRef](#)]
32. Hussien, A.A.; Abdullah, M.Z.; Yusop, N.M.; Al-Kouz, W.; Mahmoudi, E.; Mehrali, M. Heat transfer and entropy generation abilities of MWCNTs/GNPs hybrid nanofluids in microtubes. *Entropy* **2019**, *21*, 480. [[CrossRef](#)] [[PubMed](#)]
33. Al-Kouz, W.G.; Kiwan, S.; Alkhalidi, A.; Sari, M.E.; Alshare, A. Numerical study of heat transfer enhancement for low-pressure flows in a square cavity with two fins attached to the hot wall using Al<sub>2</sub>O<sub>3</sub>-air nanofluid. *Strojniški Vestnik J. Mech. Eng.* **2018**, *64*, 26–36.
34. Al-Kouz, W.; Al-Muhtady, A.; Owhaib, W.; Al-Dahidi, S.; Hader, M.; Abu-Alghanam, R. Entropy generation optimization for rarified nanofluid flows in a square cavity with two fins at the hot wall. *Entropy* **2019**, *21*, 103. [[CrossRef](#)]
35. Hussien, A.A.; Al-Kouz, W.; Yusop, N.M.; Abdullah, M.Z.; Janvekar, A.A. A Brief Survey of Preparation and Heat Transfer Enhancement of Hybrid Nanofluids. *Stroj. Vestn. J. Mech. Eng.* **2019**, *65*, 441–453. [[CrossRef](#)]
36. Nield, D.A.; Bejan, A. *Convection in Porous Media*; Springer: New York, NY, USA, 2017.
37. Esfe, M.H.; Arani, A.A.A.; Rezaie, M.; Yan, W.M.; Karimipour, A. Experimental determination of thermal conductivity and dynamic viscosity of Ag-MgO/water hybrid nanofluid. *Int. Commun. Heat Mass Transf.* **2015**, *66*, 189–195. [[CrossRef](#)]

38. Oztop, H.F.; Abu-Nada, E. Numerical study of natural convection in partially heated rectangular enclosures filled with nanofluids. *Int. J. Heat Fluid Flow* **2008**, *29*, 1326–1336. [[CrossRef](#)]
39. Mehryan, S.A.; Kashkooli, F.M.; Ghalambaz, M.; Chamkha, A.J. Free convection of hybrid MgO-Ag water nanofluid in a differentially heated porous cavity. *Adv. Powder Technol.* **2017**, *28*, 2295–2305. [[CrossRef](#)]
40. Woods, L.C. *Thermodynamics of Fluid Systems*; Oxford University Press: Oxford, UK, 1975.
41. Calcagni, B.; Marsili, F.; Paroncini, M. Natural convective heat transfer in square enclosures heated from below. *Appl. Therm. Eng.* **2005**, *25*, 2522–2531.
42. Ghasemi, B.; Aminossadati, S.M.; Raisi, A. Magnetic field effect on natural convection in a nanofluid-filled square enclosure. *Int. J. Therm. Sci.* **2011**, *50*, 1748–1756. [[CrossRef](#)]